Chemical Engineering Journal 420 (2021) 129838

Contents lists available at ScienceDirect

Chemical Engineering Journal

journal homepage: www.elsevier.com/locate/cej

Atomic-scale investigation of Lithiation/Delithiation mechanism in High-entropy spinel oxide with superior electrochemical performance

Chih-Yang Huang [a], Chun-Wei Huang [b], Min-Ci Wu [a], Jagabandhu Patra [c], Thi Xuyen Nguyen [d], Mu-Tung Chang [b], Oliver Clemens [e], Jyh-Ming Ting [d,*], Ju Li [f], Jeng-Kuei Chang [a,*], Wen-Wei Wu [a,g,h,*]

[a] Department of Materials Science and Engineering, National Chiao Tung University, Hsinchu 30010, Taiwan
[b] Material and Chemical Research Laboratories, Industrial Technology Research Institute, Hsinchu 31040, Taiwan
[c] Hierarchical Green-Energy Materials (Hi-GEM) Research Center, National Cheng Kung University, Tainan 70101, Taiwan
[d] Department of Materials Science and Engineering, National Cheng Kung University, Tainan 70101, Taiwan
[e] Universität Stuttgart, Institut für Materialwissenschaft, Chemische Materialsynthese, Heisenbergstraße 3, 70569 Stuttgart, Germany
[f] Department of Nuclear Science and Engineering and Department of Materials Science and Engineering, Massachusetts Institute of Technology, Cambridge, MA 02139, USA
[g] Intelligent Semiconductor Nanosystem Technology Research Center, Hsinchu 30078, Taiwan
[h] Frontier Research Center on Fundamental and Applied Sciences of Matters, National Tsing Hua University, Hsinchu 30013, Taiwan

ARTICLE INFO

Keywords:
High-resolution electron microscopy
Electron energy-loss spectroscopy
Spinel anode materials
Phase segregation
Lithium-ion batteries
Cycling stability

ABSTRACT

Transition-metal high-entropy oxides (HEOs) are promising electrode materials for lithium-ion batteries (LIBs) due to their superior electrochemical properties and excellent long-term cycling stability. The performance of HEOs for LIBs is highly correlated with their microstructures, especially their evolution during charging/discharging. However, there is limited information regarding this topic in the literature. In this study, the unique transition behavior of a spinel HEO, $(CrMnFeCoNi)_3O_4$, at various states of charge and cycle numbers is examined in detail for the first time. Although the elemental segregation of lithiated HEO particles is observed, the crystal structure remains spinel, leading to great cyclability. Mn nanocrystals form at 0.5 V lithiation and metallic Cr, Fe, Ni, and Co particles form at 0.01 V lithiation. The spinel $Cr_xFe_{3-x}O_4$ and $LiNi_xCo_{1-x}O_2$ phases act as seeds that grow by devouring surrounding metal nanoparticles during delithiation. The Mn can reversibly move at least dozens of nanometers across the oxide during lithiation/delithiation. The detailed cycling mechanism is examined using electron energy-loss spectroscopy. The reversible valence state variations of the constituent elements are observed. The results provide an in-depth understanding of the fundamental lithiation/delithiation mechanism of HEO, which will facilitate the development of better multi-element HEOs for Li^+ storage applications.

1. Introduction

Lithium-ion batteries (LIBs) have attracted increasing attention for application in the expanding market for electric vehicles and electronic devices due to their excellent charge storage performance, such as long cycle life, high energy and power capability, and low maintenance cost [1–3]. Novel electrode materials are required to further increase the energy density and long-term cycling stability of LIBs [4,5]. In recent years, transition metal oxides (TMOs) have become one of the most attractive electrode materials for next-generation LIBs owing to their high capacity, which results from multi-electron transfer redox reactions [6–8]. Compared to the conventional graphite anode, a TMO-based anode can operate at a higher potential, which improves safety [7,9]. TMOs such as Co_3O_4 [10], Fe_3O_4 [11], Fe_2O_3 [12], $NiFe_2O_4$ [13] and $Cu_2Nb_{34}O_{87}$ [14] are candidates for advanced LIBs. However, some issues must still be overcome for TMOs. Unsatisfactory cyclability is the major hurdle that restricts the application of traditional TMOs for LIBs [15]. Structural destruction is the root cause of electrode performance deterioration. Further material modifications of TMOs and an understanding of the underlying operation mechanism are essential and

* Corresponding authors at: Department of Materials Science and Engineering, National Chiao Tung University, Hsinchu 30010, Taiwan (W.-W. Wu).
E-mail addresses: jting@mail.ncku.edu.tw (J.-M. Ting), jkchang@nctu.edu.tw (J.-K. Chang), wwwu@mail.nctu.edu.tw (W.-W. Wu).

https://doi.org/10.1016/j.cej.2021.129838
Received 18 February 2021; Received in revised form 2 April 2021; Accepted 11 April 2021
Available online 17 April 2021

urgently needed.

Recently, high-entropy materials have drawn great interest owing to their unique properties for a wide range of applications [16–18]. Their high configurational entropy stabilizes the microstructure [17,19,20]. The concept of high entropy has been integrated with TMOs. Previous studies have shown that the advantages of transition-metal high-entropy oxides (TM-HEOs) are excellent cycling stability and rate capability for application as anode materials for LIBs [7,21]. Owing to the high entropy, the lattice structure could be maintained during cycling, which contributed to the smaller volume variation than other transition metal oxides. The higher structural stability would be beneficial for the long cycling stability due to less damage caused by volume expansion. TM-HEOs could be important anode materials for future LIBs. Apparent electrochemical performance is derived from the microstructural evolution of electrode materials during charging/discharging [10,22–26]. Unfortunately, there is limited fundamental research on TM-HEO microstructure variation during energy storage reactions. Previous studies have used X-ray diffraction (XRD) to examine the crystal structures of HEOs [7,17,19]. However, XRD has a relatively low spatial resolution. Low-resolution microstructure analyses, such as those conducted using XRD and conventional electron microscopy, do not provide detailed mechanistic information. A more advanced technique is required to gain an atomic-scale understanding of the microstructure evolution of TM-HEOs under various degrees of lithiation/delithiation.

Transmission electron microscopy (TEM) is one of the most powerful tools for examining material transformation behavior at the atomic scale due to its high resolution [27,28]. The electrode charging/discharging cycling is accompanied by material redox reactions. To precisely probe the cycling mechanism, the identification of material valence states is crucial [29,30]. Electron energy-loss spectroscopy (EELS) can provide information on oxidation states [31,32] of electrode materials upon lithiation/delithiation. Moreover, EELS can map the elemental distribution at a high resolution. The combination of scanning transmission electron microscopy (STEM) and EELS is particularly powerful [31]. The present study uses TEM, STEM, and EELS to examine the microstructure and valence state evolution of TM-HEOs for Li^+ storage.

The rock-salt type and spinel type HEOs have been explored as electrode materials for high-performance LIBs; however, rock-salt HEOs faced the problem of in active oxides, which would not contribute to the reversibly capacity [7,15,19]. The spinel structure is known to provide effective Li^+ transport paths [9,33]. The oxygen vacancies induced by the multiple valence states of cations in spinel HEO promote Li^+ conduction. In terms of the choice of the elements, the cations in $(CrMnFeCoNi)_3O_4$ are because of their similar ionic radii, which results in high-entropy-induced phase stabilization effects. Spinel HEO is a promising electrode material for next-generation LIBs, and thus a detailed atomic-level mechanistic investigation on its microstructure transition during charging/discharging is important.

In this work, the phase conversion behavior of spinel HEO at the atomic scale is explored for the first time. The atomic-level microstructures at various states of charge are identified using high-resolution TEM (HRTEM). Moreover, the redox sequence and valence state variation of the constituent elements of HEO are examined via STEM/EELS. The high reversibility of the structural evolution explains the great cyclability of the HEO electrode. The combined microstructure and valence state information allows an in-depth understanding of the HEO charge-storage mechanism and will contribute to the design of better HEOs for LIB applications.

2. Experimental section

2.1. Synthesis of spinel HEO powder

$Cr(NO_3)_3{\cdot}9H_2O$ (Alfa Aesar, 98.5%), $Mn(NO_3)_2{\cdot}6H_2O$ (Alfa Aesar, 98.5%), $Fe(NO_3)_3{\cdot}9H_2O$ (J.T. Baker, 99%), $Co(NO_3)_2{\cdot}6H_2O$ (J.T. Baker, 99%), and $Ni(NO_3)_2{\cdot}6H_2O$ (Alfa Aesar, 98.5%) precursors with concentrations of 0.75, 2, 0.5, 2, and 1 mM, respectively, were used to synthesize spinel HEO powder via a surfactant-assisted hydrothermal method. (1-Hexadecyl)trimethylammonium bromide (CTAB, Alfa Aesar, 98.5%) was used as the surfactant. The precursors were dissolved in 40 ml of deionized water with 1.25 ml of CTAB. Then, urea was added to the solution at a molar ratio of urea to total metal of 6:1. The resulting solution was transferred into an autoclave and subjected to a hydrothermal treatment at 140 °C for 5 h. The precipitate was collected via centrifugation. After washing with ethanol and deionized water, the powder was dried at 80 °C for 12 h. Finally, the obtained powder was heat-treated under air at 900 °C for 2 h at a heating rate of 10 °C/min. The Fe, Cr, Co, Ni, and Mn content in the HEO, measured using inductively coupled plasma-mass spectrometry, was 8.0%, 11.2%, 30.2%, 22.0%, and 28.6%, respectively. The configurational entropy of our HEOs is 1.5 R where R is the gas constant.

2.2. Preparation of electrodes and cells

The spinel HEO powder, carbon black, and poly(vinylidene fluoride) at a weight ratio of 7:2:1 were mixed in *N*-methyl-*2*-pyrrolidone solution, and the resulting mixture was pasted onto Cu foil and dried at 100 °C for 7 h. The electrode was then roll-pressed and punched to fit the size of a CR2032 coin cell. A diethyl carbonate and ethylene carbonate (1:1 by volume) mixed solvent with 1 M $LiPF_6$ was used as the electrolyte. The counter electrode and separator were Li foil and a glass fiber membrane, respectively. The cell assembly was conducted in an Ar-filled glove box (Innovation Technology Co. Ltd.) with moisture and oxygen content levels below 0.3 ppm. The charge–discharge properties of the cells were evaluated using a battery tester (Arbin BT-2043) under various current densities.

2.3. Sample preparation for TEM, STEM, and EELS analyses

The pristine HEO powder was dispersed in anhydrous alcohol and then dropped onto a Cu grid coated with lacey carbon film. The cycled samples were scratched off the electrodes in the glove box, dispersed in anhydrous alcohol, and then placed on TEM grids supported by lacey carbon film. The grid was then mounted into the TEM holder and loaded in a pumping station to allow anhydrous alcohol to evaporate, followed by loading into the TEM chamber. The HRTEM analyses were performed using a JEOL F200 electron microscope equipped with an X-ray energy-dispersive spectroscopy (EDS) system. The valence states of the HEO constituent elements at various states of charge were characterized using EELS combined with Cs-corrected STEM (JEOL ARM 200F).

3. Results and discussion

The microstructural identification of the pristine spinel HEO is shown in Fig. 1. The dark-field STEM image reveals that the HEO particles consisted of multiple grains. Fig. 1b shows the lattice image of a grain along its [3 3 2] zone. The grain size is larger than that of the rock-salt HEO reported in the literature [19]. According to the EDS mapping data (Fig. 1c-h), Fe, Cr, Co, Ni, Mn, and O are uniformly distributed over the oxide particle. The XRD pattern (Fig. 1i) confirms that the synthesized powder is single-phase spinel HEO. The detail Rietveld analysis is shown in Table S1 and Figure S1. The HRSTEM image and the atomic EELS mapping were shown in Figure S2. It demonstrated that the actual atomic position and the elemental distribution of multi atoms, indicating that each column of atoms contained all kinds of metal atoms.

To reveal the detailed microstructure evolution during lithiation/delithiation, samples with various degrees of charge were selected for TEM analyses. According to the charge–discharge curves shown in Fig. 2a, the lithiation process at the first cycle consists of two steps. The first step finishes at approximately 0.5 V versus Li^+/Li and then further lithiation takes place until the cut-off potential of 0.01 V. Accordingly, 0.5 and 0.01 V were chosen as the potentials of interest for the

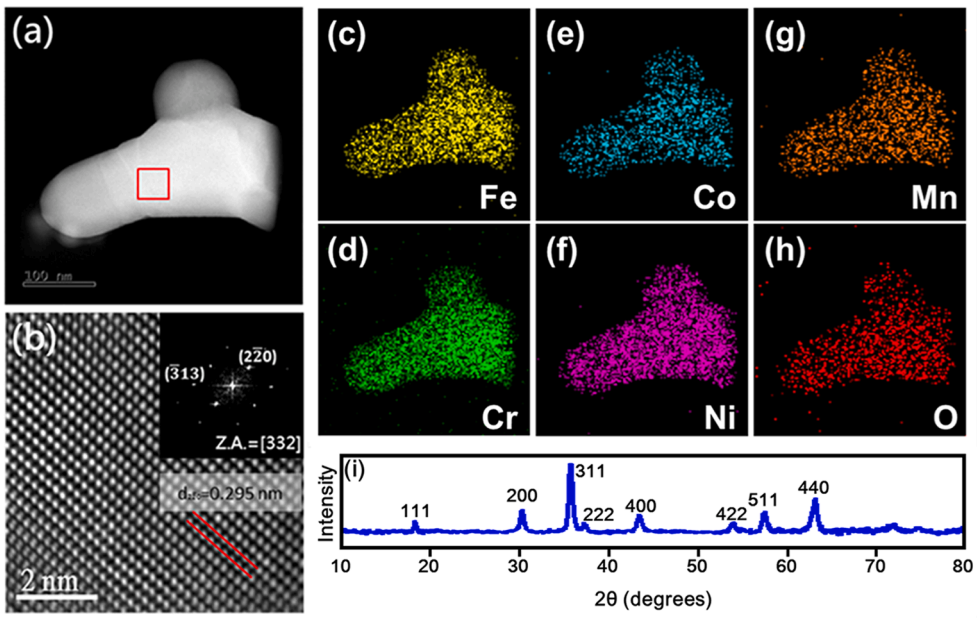

Fig. 1. Structure identification and elemental distribution of pristine HEO. (a) Dark-field STEM image of HEO particle. (b) HRTEM image of HEO. EDS mapping results showing uniform elemental distribution of (c) Fe, (d) Cr, (e) Co, (f) Ni, (g) Mn, and (h) O. (i) XRD pattern of HEO.

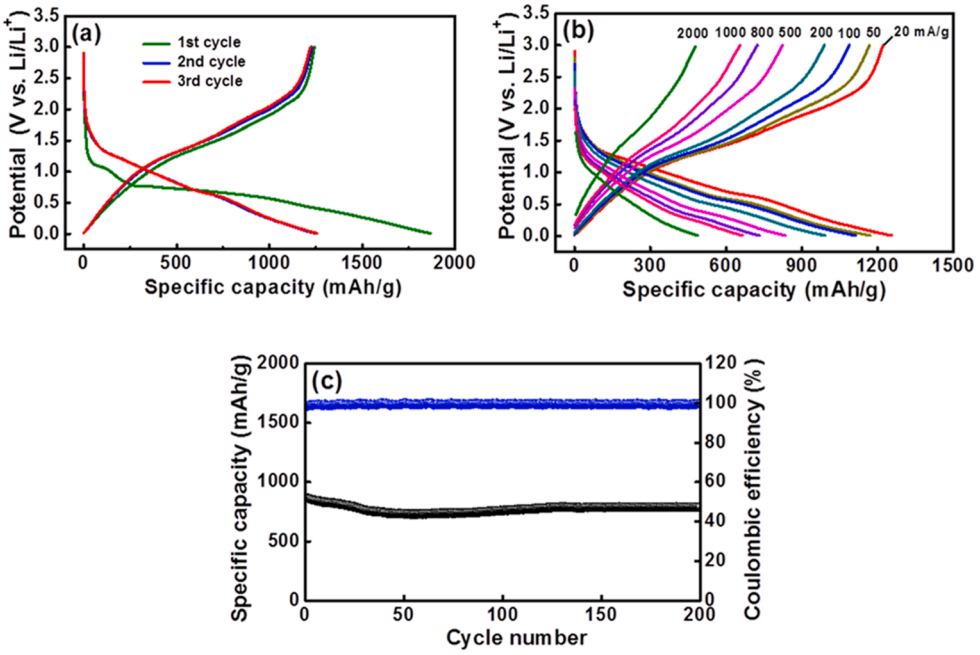

Fig. 2. Electrochemical Li^+ storage properties of spinel HEO electrode. (a) Initial charge–discharge curves recorded at 20 mA g^{-1}. (b) Electrode rate capability evaluated at various specific currents. (c) Cycling stability of electrode measured at 500 mA g^{-1}.

microstructure analyses. A specimen that was fully lithiated and then delithiated up to 3 V was also examined. As shown in Fig. 2a, the charge–discharge curves almost overlap from the second cycle onward. To study the structural evolution reversibility of the HEO, specimens obtained after the second lithiation and delithiation were also analyzed. Fig. 2b shows the charge–discharge curves of the HEO electrode measured at various current densities. The measured reversible capacities are 1225, 1170, 1090, 990, 825, 725, 655, and 485 mAh g^{-1} at 20, 50, 100, 200, 500, 800, 1000, and 2000 mA g^{-1}, respectively. The theoretical capacity is 965.62 (mAh/g), meaning that the measured capacities at the low rates contained an extra capacities. The reason for the extra capacity is owing to the magnetic metal atoms after lithiation. Previous study reported that the lithiated magnetic metal atoms (such as Fe, Co and Ni) would store a large number of spin-polarized electrons during discharging at low potentials, which caused the extra capacity [8]. The mechanism during cycling was clarified as: $Fe + 3LiF \rightleftharpoons FeF_3 + 3Li^+ + 3e^-$ [34]. Fig. 2c shows the cycling stability of the HEO electrode measured at 500 mA g^{-1}. After 200 charge–discharge cycles, the electrode showed a capacity retention ratio of ~ 91% with a Coulombic efficiency value of more than 99%. This remarkable cyclability is explained later from a microstructure point of view. Compared to the equimolar high-entropy $(CrMnFeCoNi)_3O_4$ [7], the performance in our

study (non-equimolar) is better. The multi-valence nature of the constituent elements in the high entropy oxide regulates the formation of oxygen vacancies, which are known to be favorable for Li^+ transport and thus give high-rate charge–discharge capability [21]. Based on the definition of high entropy materials (contained five or more elements and the concentration of each of the element ranges from 5 to 35% or S≧1.5R) [35], the non-equimolar HEO in this study maintain the characteristics of high entropy materials and provided the better performance. Higher configurational entropy of equimolar HEO resulted in better phase stabilization effect, which might be a factor restrict the redox reaction during cycling and performances.

The top panel of Fig. 3 shows results for an HEO sample subjected to the first 0.5-V lithiation. The dark-field STEM image (Fig. 3a) shows that many nanograins formed in the HEO particle, which is quite different from the initial large grains shown in Fig. 1a. In contrast to the uniform elemental distribution of the pristine HEO particles, the STEM EELS mapping data (Fig. 3b-g) reveal that the elements became segregated upon lithiation. The EELS mapping results reveal several aspects. First, the distributions of Fe and Cr almost overlap, indicating that Cr and Fe are present in the same regions. Second, Co and Ni are coherent but separate from the Fe/Cr-rich domains, whereas the O signals are uniformly distributed across the sample. Finally, the distribution of Mn is distinct from those of the other elements. Fig. 3h shows a TEM image of the orange square region in Fig. 3a. The blue line represents the boundary between the Fe/Cr-rich and Co/Ni-rich domains. The HRTEM images and the corresponding fast Fourier transform (FFT) patterns reveal that the crystal structures of both domains remain spinel (Fig. 3i-j), the same as that of the pristine HEO. The Fe/Cr-rich domain was identified as a spinel $Cr_xFe_{3-x}O_4$ phase. The domain containing Co and Ni was identified as spinel $LiNi_xCo_{1-x}O_2$, a phase that has also been found for layered Li-Ni-Co oxide after excessive delithiation [36]. The combination of EELS mapping and HRTEM techniques clearly differentiates the HEO, $Cr_xFe_{3-x}O_4$, and $LiNi_xCo_{1-x}O_2$ phases, which have the same crystal structure and similar lattice constants. In the pristine spinel HEO, the metal lattice points were randomly occupied by Fe, Cr, Co, Ni, and Mn atoms [37]. At 0.5-V lithiation, phase segregation into two new spinel phases, namely $Cr_xFe_{3-x}O_4$ and $LiNi_xCo_{1-x}O_2$, occurred. Fig. 3k shows that the Mn-rich area contains metallic Mn nanocrystals.

The HEO sample subjected to further lithiation (down to 0.01 V) is shown in the bottom panel of Fig. 3. The nanogranular microstructure was retained. As shown in Fig. 3m-r, the elemental distributions are very similar to those found for 0.5 V (i.e., Cr/Fe-rich and Co/Ni-rich domains separate from the metallic Mn region). However, as confirmed by the HRTEM images and corresponding FFT patterns in Figure S3, the 0.01-V-lithiated sample retained the spinel matrix, which is composed of $Cr_xFe_{3-x}O_4$ and $LiNi_xCo_{1-x}O_2$ phases. We also found that all metals except for the Mn nanocrystals were reduced in this step. Because the *d* spacing values of the metals are very similar, we measured the spacing by adopting multiple planes and calculating the average *d* distance. The included angles between two crystal planes and the chemical composition

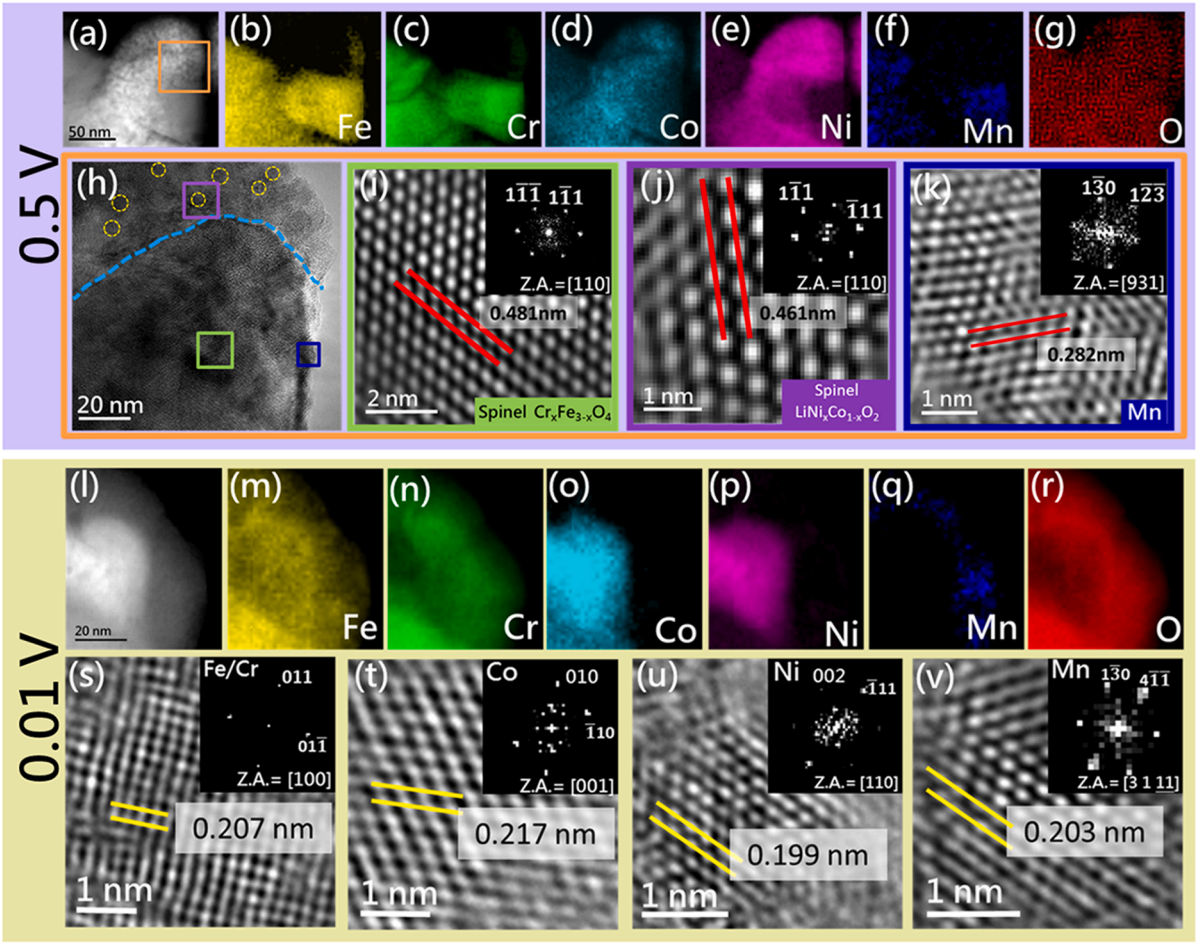

Fig. 3. Structure identification and elemental distribution of HEO particles lithiated at 0.5 and 0.01 V. (a) Dark-field STEM image of HEO particle lithiated at 0.5 V. EELS mapping results showing elemental distribution of (b) Fe, (c) Cr, (d) Co, (e) Ni, (f) Mn, and (g) O at 0.5 V. (h) HRTEM image of orange square region in (a). The yellow dashed lines mark nanograins formed after lithiation and the blue dashed line indicates the boundary between Fe/Cr-rich and Co/Ni-rich domains. HRTEM images of (i) $Cr_xFe_{3-x}O_4$, (j) $LiNi_xCo_{1-x}O_2$, and (k) Mn phases. (l) Dark-field STEM image of HEO particle lithiated at 0.01 V. EELS mapping results showing elemental distribution of (m) Fe, (n) Cr, (o) Co, (p) Ni, (q) Mn, and (r) O at 0.01 V. HRTEM images of metallic (s) Fe/Cr, (t) Co, (u) Ni, and (v) Mn.

information were also taken into account. Metallic Cr and Fe both have a body-centered cubic structure and have similar lattice constants. Therefore, it is difficult to exactly differentiate the Cr and Fe HRTEM lattice images, as shown in Fig. 3s. Nevertheless, based on the chemical composition analysis results, we believe that both Fe and Cr metal particles were present. In the Co/Ni-rich domain, the hexagonal close-packed nanocrystals with an average *d* spacing of 0.217 nm refer to metallic Co (Fig. 3t) and the face-centered-cubic nanocrystals with an average *d* spacing of 0.199 nm refer to metallic Ni (Fig. 3u). The STEM EELS mapping results in Fig. 3m-p suggest that the metallic Cr and Fe nanocrystals precipitated around the $Cr_xFe_{3-x}O_4$ grains and that the metallic Co and Ni nanocrystals precipitated around the $LiNi_xCo_{1-x}O_2$ grains because the Cr/Fe and Co/Ni elemental distributions are well separated. Fig. 3v confirms the existence of Mn metal nanoparticles. This is the first work to thoroughly examine the formation and distribution of various metallic nanocrystals produced after the lithiation of HEO. Due to the low quantity and tiny size of the metallic particles, it is difficult to characterize them using regular XRD and even traditional TEM techniques. Moreover, the very similar *d* spacing values of the constituent metals make distinguishing nanocrystals with various elements difficult. Here, we provide a methodology with an atomic-scale resolution for probing the detailed HEO microstructure evolution at various degrees of electrochemical lithiation.

It is remarkable that the elements segregated after the lithiation process. Previous study reported that the element separation commonly occurred in the system of transition metal oxides during cycling, which is related to the corrosion phenomenon caused by the electrolyte[38]. It was suggested that the corrosion phenomenon had a promoting effect on the element segregation, resulting in Mn being separated with other elements. Additionally, according to the table of binary spinel oxides formation energy shown in Table S2 [39,40], the formation energy of $Cr_xFe_{3-x}O_4$ is the lowest. Forming $Cr_xFe_{3-x}O_4$ would make the Gibbs free energy smaller and the reaction would tend to form it. The separated Co and Ni became the phase found in the system of Li-Ni-Co oxide after cycling, $LiNi_xCo_{1-x}O_2$ [36].

To study the HEO structural reversibility, a sample subjected to lithiation (until 0.01 V) and then delithiation (up to 3 V) was examined. The obtained data are shown in Fig. 4. As shown in Fig. 4b, the sample contains many spinel nanograins; however, their lattice parameters are different from those of the pristine HEO, indicating that the HEO crystals did not fully recover. The chemical composition mapping results in Fig. 4c-h reveal the segregation between the Fe/Cr and Ni/Co domains. It was confirmed that the Fe/Cr-rich region is composed of the $Cr_xFe_{3-x}O_4$ phase (Fig. 4i), whereas the Ni/Co-rich region is composed of the $LiNi_xCo_{1-x}O_2$ phase (Fig. 4j). Interestingly, it was found that the distribution of Mn overlapped with that of Fe/Cr. Presumably, during delithiation, the Mn oxidized and became integrated with the spinel $Cr_xFe_{3-x}O_4$ phase (i.e., forming $Mn_xCr_yFe_{3-x-y}O_4$). There were no metallic nanocrystals observed at this stage.

EELS analyses were performed to further examine the reaction mechanism. The white-line intensity ratio between L_3 and L_2 is commonly utilized to define the valence states of elements. Moreover, an EELS peak shift can indicate oxidation/reduction processes [31]. Fig. 5 shows the EELS spectra of all elements at various states of charge. From the pristine state to the 0.5-V lithiation, the Cr and Mn peaks shifted to lower energy levels. According to the white-line intensity ratios, the valence state of Cr transformed from + 3 to + 2 [41], and that of Mn transformed from the mixed + 2/+3 to 0 [31]. In contrast, Fe, Co, and Ni did not show a significant valence change in this step. Further lithiation (to 0.01 V) caused the L_3 peaks of Cr, Fe, Co, and Ni to shift

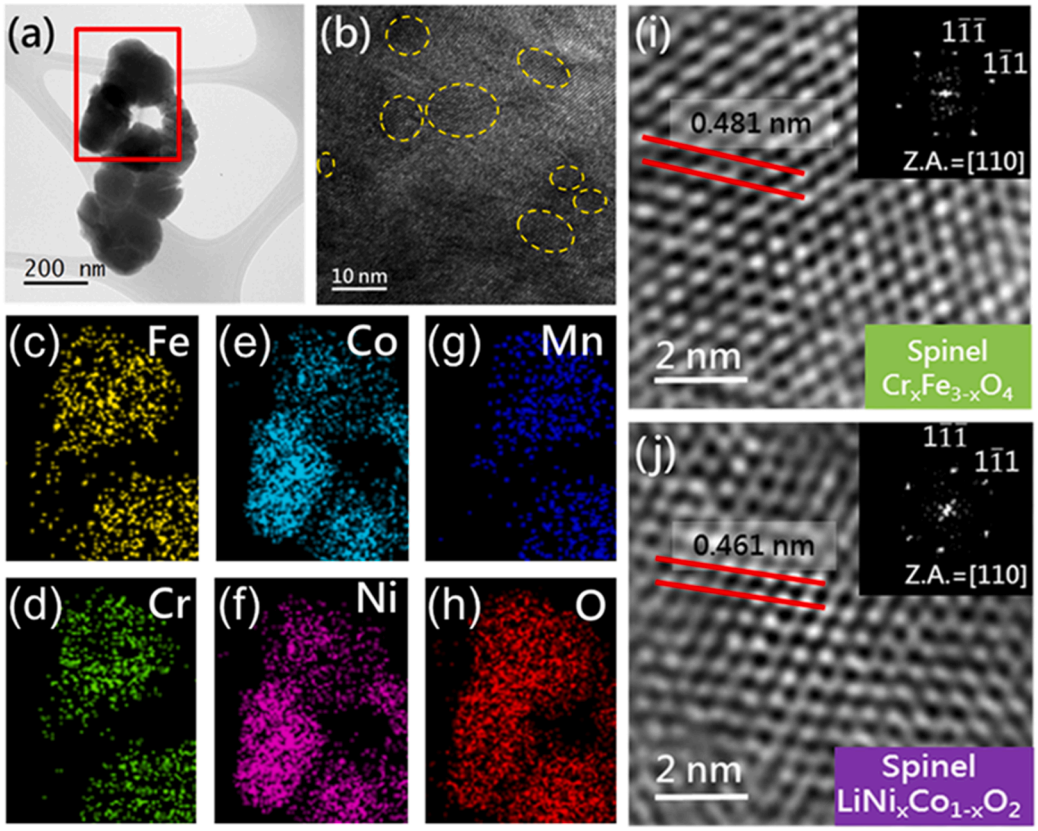

Fig. 4. Structure identification and elemental distribution of HEO particles after first delithiation. (a) TEM image of HEO particle after first delithiation. (b) HRTEM image showing spinel nanograins (marked by yellow dashed lines). EDS mapping results showing elemental distribution of (c) Fe, (d) Cr, (e) Co, (f) Ni, (g) Mn, and (h) O in red square region of (a). HRTEM images of (i) $Cr_xFe_{3-x}O_4$ and (j) $LiNi_xCo_{1-x}O_2$ phases.

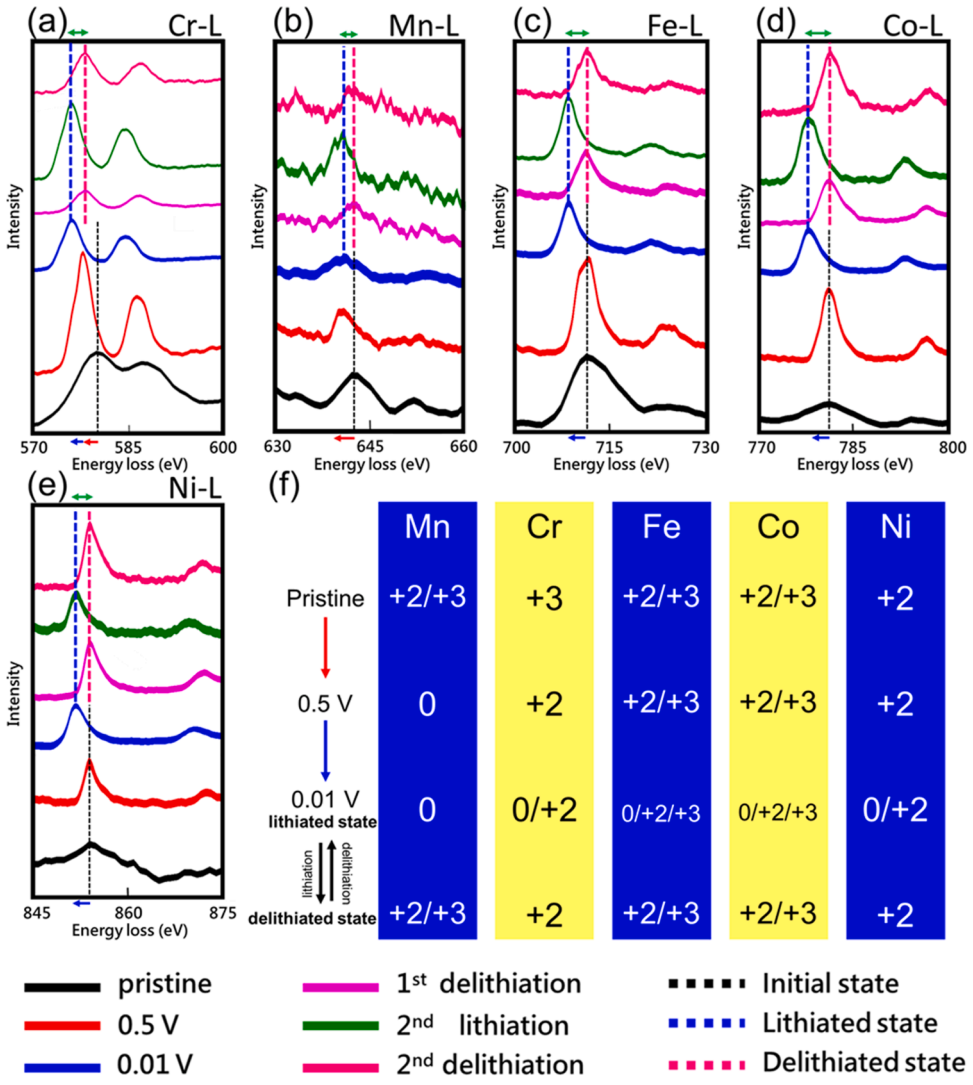

Fig. 5. EELS analysis results of HEO samples at various states of charge and cycle numbers. EELS L-edge spectra of (a) Cr, (b) Mn, (c) Fe, (d) Co, and (e) Ni elements. The red and blue arrows at bottom of × axes indicate energy shift from pristine to 0.5 V and from 0.5 to 0.01 V, respectively. (f) Summary of valence state variations of constituent elements of HEO.

toward lower energy. Cr was further reduced from + 2 to mixed 0/+2 [13,41]. Both Fe and Co were identified as mixed + 2/+3 in the pristine state and the 0.5-V lithiated state according to their white-line ratios [42]. They transformed to mixed 0/+2/+3 at 0.01 V. For Ni, the pristine valence was + 2 in the HEO [13,41] and reduced to 0/+2 after 0.01-V lithiation. Upon delithiation, the metallic Mn oxidized, transforming to + 2/+3 valence. Except for Mn, the valence states of the elements switched back to those of the 0.5 V lithiated state, as shown in Fig. 5f. The EELS analysis results well agree with the TEM microstructure observations.

Figure S4 shows the microstructure of a sample after the second-cycle lithiation (0.01 V). Besides the spinel nano-domains, metallic Fe, Cr, Co, Ni, and Mn nanoparticles were observed. The obtained microstructures and crystallinity are similar to those found after the first lithiation (bottom panel of Fig. 3), indicating great structural reversibility. Figure S5a shows the large-area diffraction patterns of the samples after lithiation and delithiation at the first and second cycles. Diffraction rings attributed to the spinel structure are consistently present. Figure S5b reveals that the produced spinel $Cr_xFe_{3-x}O_4$ and $LiNi_xCo_{1-x}O_2$ phases have *d* spacing values similar to those of the pristine spinel HEO. This stable $Cr_xFe_{3-x}O_4/LiNi_xCo_{1-x}O_2$ spinel framework is thought to be responsible for the great cyclability of the HEO electrode shown in Fig. 2c. For traditional (i.e., low-entropy) spinel oxides, such as Co_3O_4 and $NiFe_2O_4$, the spinel crystal structures are completely destroyed after the first lithiation [10,13]. High-entropy-induced phase stabilization effects were observed for our HEO. It is also noted that, as shown in Figure S5a, the Li_2O signal always appeared, suggesting that the spinel nanograins and metallic nanocrystals were surrounded by a Li_2O phase. The Cr, Mn, Fe, Co, and Ni EELS spectra obtained upon cycling are shown in Fig. 5. The spectra obtained at the first and second lithiation steps are similar. The spectra acquired after the first delithiation step are similar to those acquired after the second delithiation step. These results indicate high reversibility in terms of the valence state variation of the HEO electrode. As shown in Fig. 5f, the Mn valence cycled between 0 (under lithiation) and + 2/+3 (under delithiation). The valence states of Cr and Ni cycled between 0/+2 and + 2 and those of Fe and Co cycled between 0/+2/+3 and + 2/+3. According to the EELS results, all elements' valences switched back to pristine state after total delithiation except for Cr. The reason we supposed for the valences of Cr switch only back to + 2 was related to the lithiated products. In the lithiated spinel oxides of $Cr_xFe_{3-x}O_4$, the energy for Cr^{2+} oxidizing Cr^{3+} is + 0.42 eV. However, the energy for Fe^{2+} oxidizing Fe^{3+} is −0.77 eV, which is lower than Cr^{2+} [43]. From this viewpoint, oxidizing Fe would reach lower Gibbs free energy.

Figure S6 showed the XRD patterns at different states, which displayed the crystallinity at macro scale. The spinel phase intensity gradually decreased upon cycling, indicating that the long-range crystallinity of the spinel structure diminished. However, the short-range ordered nanocrystals which firstly detailed discussed in this study still preserved, as confirmed by the atomic-scale TEM analyses.

Because the amount of the residual spinel oxides could not be precisely identified, the stoichiometric detailed electrochemical reaction equations would not be defined. This is a common problem in the HEO systems [7,15]. Instead, the electrochemical reaction equations could be described by the species, which also reported in the previous HEO study. The reaction equation of species could be described as:

First lithiation:

Spinel-HEO(M) + 2Li → Spinel $(CrFe)_3O_4$ + Spinel $Li(CoNi)O_2$ + M + Li_2O

Delithiation/ lithiation cycling:

Spinel $(CrFe)_3O_4$ + Spinel $Li(CoNi)O_2$ + M + Li_2O ⇌ **Spinel $(CrFe)_3O_4$ + Spinel $Li(CoNi)O_2$** + 2Li

where M includes Cr, Mn, Fe, Co and Ni.

Based on the above analysis results, the microstructure evolution and reaction mechanism of the HEO toward Li^+ storage are schemed in Fig. 6 and Figure S7. At the macroscale (Figure S7), the pristine HEO turns into the spinel $Cr_xFe_{3-x}O_4$ and $LiNi_xCo_{1-x}O_2$ phases together with dispersed Mn nanocrystals at shallow lithiation. Further lithiation leads to the formation of metallic Cr, Fe, Co, and Ni nanoparticles. The two spinel phases and various metal particles are embedded in a Li_2O matrix, which forms during the first lithiation and acts as a buffer layer that accommodates the volume variation of the electroactive species during subsequent redox cycles. At the atomic scale (Fig. 6), the pristine HEO has a spinel structure, whose metal lattice points are randomly occupied by Fe, Cr, Co, Ni, and Mn atoms (Fig. 6a). Upon lithiation to 0.5 V, the original metal − O bonding begins to be rearranged (Fig. 6b), and the pristine large-grain HEO segregates into two new spinel phases (i.e., $Cr_xFe_{3-x}O_4$ and $LiNi_xCo_{1-x}O_2$) with nanograins and Mn nanoparticles (Fig. 6c). The pristine HEO, $Cr_xFe_{3-x}O_4$, and $LiNi_xCo_{1-x}O_2$ all have similar lattice parameters. The phase segregation was for the first time revealed here using a combination of HRTEM, STEM, and EELS techniques. Continued lithiation to 0.01 V leads to precipitation of metallic Fe and Cr nanocrystals from $Cr_xFe_{3-x}O_4$ and the precipitation of metallic Ni and Co nanocrystals from $LiNi_xCo_{1-x}O_2$, while the spinel-structure framework is preserved (Fig. 6d,e). During delithiation (Fig. 6f,g), the residual spinel oxides act as seeds that grow by devouring surrounding metal nanoparticles. It was found that the separated metallic Mn during lithiation can move toward and then become integrated with the $Cr_xFe_{3-x}O_4$ phase. The Mn can reversibly move at least dozens of nanometers across the oxide during lithiation/delithiation. Due to the small size of $Cr_xFe_{3-x}O_4$ and Mn grains and ample free volume/vacancies, the oxygen sublattice may gain mobility upon delithiation and envelop the Mn atoms or the Mn atoms may diffuse into the oxide lattice [44,45]. In cases of traditional transition metal oxides, the lattice structure of as-synthesized electrode materials could not be maintained after cycling. This lead to the understanding for traditional transition metal oxides during cycling only focused on the diffusion of lithium ions. However, spinel-HEOs in this study remained the microstructure of spinel with similar lattice constant, which provided high structural stability. The reactions outlined differ from the traditional understanding for classic conversion anodes that only Li^+ ions diffuse in and out, contributing to the reversible capacity. The oxygen mobility and/or transition metal mobility in HEO could be utilized to achieve highly reversible transformation. The EELS spectrum demonstrated that the valence state of Mn would change at this step, which also contributing to the reversible capacity. In other words, it indicated that the oxygen mobility and/or transition metal mobility would be also contributing to the reversible capacity, which differed from the classic conversion anodes. The next lithiation cycle again reduces the spinel phases and leads to the formation of various metallic nanocrystals (Fig. 6h,e). The microstructure reversibly cycles between the structures shown in Fig. 6e and Fig. 6h during repeated charging/discharging. The reason we supposed for the reaction stopping at spinel oxides ($Cr_xFe_{3-x}O_4$ and $LiNi_xCo_{1-x}O_2$) is owing to the high-entropy stabilization effect of HEOs, which was also discovered in previous studies [17,19]. The high configurational entropy is helpful for maintaining the lattice structure, leading to high structural stability.

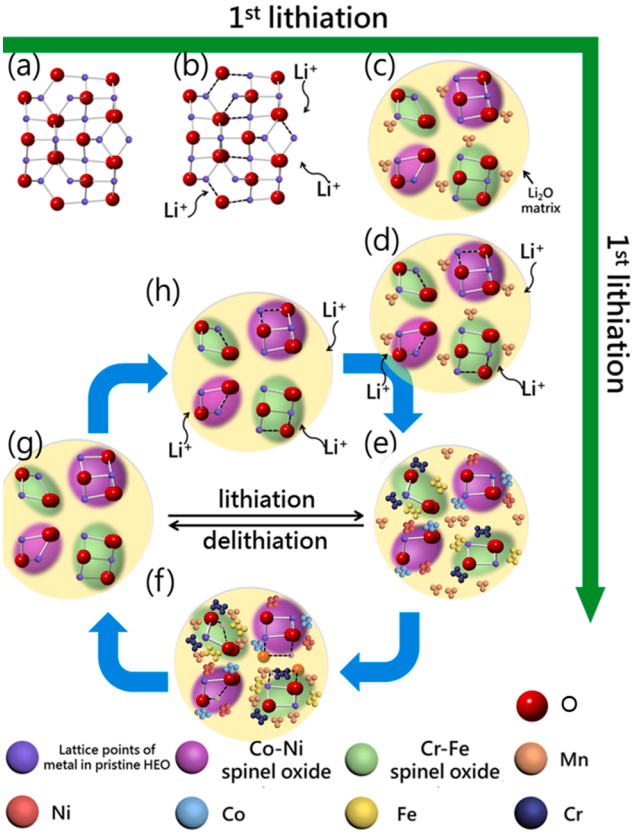

Fig. 6. Schematic illustration of atomic-scale microstructure evolution of HEO during lithiation/delithiation cycling. (a) Cr, Fe, Co, Ni, and Mn atoms are randomly distributed in HEO metal lattice. (b) HEO segregates into $Cr_xFe_{3-x}O_4$, $LiNi_xCo_{1-x}O_2$, and metallic Mn, which are embedded in (c) Li_2O matrix. (d, e) Fe and Cr metal nanoparticles precipitate around $Cr_xFe_{3-x}O_4$ and Co and Ni metal nanoparticles precipitate around $Cr_xFe_{3-x}O_4$. (f,g) Metallic nanoparticles dissolve back into the spinel grains. The segregated Mn atoms move toward and become integrated with the $Cr_xFe_{3-x}O_4$ phase. The microstructure reversibly cycles between (e) and (h) during repeated charging/discharging.

Figure S8 shows SEM images of the HEO electrodes before and after 100 charge–discharge cycles (terminated at the lithiation step). Unlike conventional low-entropy transition metal oxides [7], neither significant agglomeration nor cracks were observed. The diameter expansion of the HEO particles was estimated and compared to values reported in the literature [4,5], as shown in Figure S9. The constrained volume change can be attributed to the two new spinel phases having lattice constants similar to that of the pristine HEO and being always present during charging/discharging, functioning as a dimensional stabilizer. The unique mechanism combined the structural stability and the reversibly capacities of spinel HEOs, which contributed to the good cycle stability. Moreover, the precipitated metallic nanoparticles were well dispersed around the spinel grains, which were together wrapped by Li_2O. Thus, electrode integrity was maintained after cycling. To fully verify the applications value of the HEOs anode materials, the full battery test constructed by the cathode materials and the designed method in previous study was conducted [46]. The obtained charge–discharge curves are shown in Figure S10. The results reveal great performance of the full

battery.

4. Conclusions

The conversion behavior of spinel HEO during charge–discharge cycles was investigated at the atomic scale for the first time. The phase segregation of pristine HEO into two new spinel phases, namely $Cr_xFe_{3-x}O_4$ and $LiNi_xCo_{1-x}O_2$, upon 0.5-V lithiation was confirmed. These phases were always present during lithiation/delithiation cycles, acting as a structural stabilizer and being responsible for the great electrode cyclability. The high-resolution analyses in this study identified the formation of Mn nanocrystals at 0.5-V lithiation. Fe, Cr, Co, and Ni metallic particles were observed upon further lithiation to 0.01 V. At delithiation, all the precipitated metal particles dissolved back into the spinel grains. The valence state variations of the elements were examined in detail using the EELS technique. Clear chemical shifts were observed. These shifts provide information on the reaction mechanism and chemical reversibility. It was confirmed that all the constituent elements of the HEO were actively involved in the highly reversible redox transition during Li^+ uptake/release. We demonstrated a powerful methodology for understanding the microstructure evolution at the atomic level during lithiation/delithiation of the spinel HEO electrode. The results of this study will facilitate the development of better electrode materials for energy-storage applications.

Declaration of Competing Interest

The authors declare that they have no known competing financial interests or personal relationships that could have appeared to influence the work reported in this paper.

Acknowledgements

The authors acknowledges the support from the Ministry of Science and Technology (MOST) in Taiwan (MOST 106-2628-E-009-002-MY3, MOST 106-2119-M-009-008, MOST 107-2119-M-009-019, MOST 108-2221-E-009-036-MY3, MOST 108-2218-E-006-023, MOST 109-2628-E-009-008-MY3 and MOST 110-2731-M-009-001). This work was financially supported by the "Center for Semiconductor Technology Research" from The Featured Areas Research Center Program within the framework of the Higher Education Sprout Project by the Ministry of Education (MOE) in Taiwan. This work is also supported in part by the Ministry of Science and Technology, Taiwan, under Grant MOST-109-2634-F-009-029 and MOST 110-2634-F-009-027.

Declaration of Competing Interest

The authors declare that they have no known competing financial interests or personal relationships that could have appeared to influence the work reported in this paper.

Appendix A. Supplementary data

Supplementary data to this article can be found online at https://doi.org/10.1016/j.cej.2021.129838.

References

[1] N. Peeters, K. Binnemans, S. Riaño, Solvometallurgical recovery of cobalt from lithium-ion battery cathode materials using deep-eutectic solvents, Green Chem. 22 (13) (2020) 4210–4221, https://doi.org/10.1039/D0GC00940G.
[2] Y. Sun, L.i. Wang, Y. Li, Y. Li, H.R. Lee, A. Pei, X. He, Y.i. Cui, Design of red phosphorus nanostructured electrode for fast-charging lithium-ion batteries with high energy density, Joule 3 (4) (2019) 1080–1093, https://doi.org/10.1016/j.joule.2019.01.017.
[3] X. Judez, G.G. Eshetu, C. Li, L.M. Rodriguez-Martinez, H. Zhang, M. Armand, Opportunities for rechargeable solid-state batteries based on li-intercalation cathodes, Joule 2 (11) (2018) 2208–2224, https://doi.org/10.1016/j.joule.2018.09.008.
[4] G. Chen, L. Yan, H. Luo, S. Guo, Nanoscale engineering of heterostructured anode materials for boosting lithium-ion storage, Adv. Mater. 28 (35) (2016) 7580–7602, https://doi.org/10.1002/adma.201600164.
[5] J. Xu, J. Mahmood, Y. Dou, S. Dou, F. Li, L. Dai, J.-B. Baek, 2D frameworks of C2N and C3N as new anode materials for lithium-ion batteries, Adv. Mater. 29(34) (2017) 1702007. https://doi.org/10.1002/adma.201702007.
[6] R.J. Clément, Z. Lun, G. Ceder, Cation-disordered rocksalt transition metal oxides and oxyfluorides for high energy lithium-ion cathodes, Energy Environ. Sci. 13 (2) (2020) 345–373, https://doi.org/10.1039/C9EE02803J.
[7] D. Wang, S. Jiang, C. Duan, J. Mao, Y. Dong, K. Dong, Z. Wang, S. Luo, Y. Liu, X. Qi, Spinel-structured high entropy oxide (FeCoNiCrMn)3O4 as anode towards superior lithium storage performance, J. Alloy. Compd. 844 (2020) 156158, https://doi.org/10.1016/j.jallcom.2020.156158.
[8] Q. Li, H. Li, Q. Xia, Z. Hu, Y. Zhu, S. Yan, C. Ge, Q. Zhang, X. Wang, X. Shang, S. Fan, Y. Long, L. Gu, G.-X. Miao, G. Yu, J.S. Moodera, Extra storage capacity in transition metal oxide lithium-ion batteries revealed by in situ magnetometry, Nat. Mater. 20 (1) (2021) 76–83, https://doi.org/10.1038/s41563-020-0756-y.
[9] H. Xu, H. Zhang, J. Ma, G. Xu, T. Dong, J. Chen, G. Cui, Overcoming the challenges of 5 V Spinel LiNi0.5Mn1.5O4 cathodes with solid polymer electrolytes, ACS Energy Lett. 4(12) (2019) 2871-2886. https://doi.org/10.1021/acsenergylett.9b01871.
[10] G.-M. Huang, T.-C. Tsai, C.-W. Huang, N. Kumar, T.-Y. Tseng, W.-W. Wu, Dynamic observation of reversible lithium storage phenomena in hybrid supercapacitor devices, Nano Energy 41 (2017) 494–500, https://doi.org/10.1016/j.nanoen.2017.10.002.
[11] S. Fang, D. Bresser, S. Passerini, Transition metal oxide anodes for electrochemical energy storage in lithium- and sodium-ion batteries, Adv. Energy Mater. 10 (1) (2020) 1902485, https://doi.org/10.1002/aenm.201902485.
[12] Q. Su, D. Xie, J. Zhang, G. Du, B. Xu, In situ transmission electron microscopy observation of the conversion mechanism of Fe2O3/graphene anode during lithiation–delithiation processes, ACS Nano 7(10) (2013) 9115-9121. https://doi.org/10.1021/nn403720p.
[13] G.-M. Huang, C.-W. Huang, N. Kumar, C.-Y. Huang, T.-Y. Tseng, W.-W. Wu, In situ TEM investigation of electron beam-induced ultrafast chemical lithiation for charging, J. Mater. Chem. A 8(2) (2020) 648-655. https://doi.org/10.1039/C9TA09988C.
[14] X. Cai, H. Yan, R. Zheng, H. Yu, Z. Yang, X. Zhang, M. Xia, W. Chen, Y. Cui, J. Shu, Cu2Nb34O87 nanowires as a superior lithium storage host in advanced rechargeable batteries, Inorg. Chem. Front. 8(2) (2021) 444-451. https://doi.org/10.1039/D0QI01075H.
[15] N. Qiu, H. Chen, Z. Yang, S. Sun, Y. Wang, Y. Cui, A high entropy oxide (Mg0.2Co0.2Ni0.2Cu0.2Zn0.2O) with superior lithium storage performance, J. Alloy. Compd. 777 (2019) 767–774, https://doi.org/10.1016/j.jallcom.2018.11.049.
[16] Q. Wang, A. Sarkar, D.i. Wang, L. Velasco, R. Azmi, S.S. Bhattacharya, T. Bergfeldt, A. Düvel, P. Heitjans, T. Brezesinski, H. Hahn, B. Breitung, Multi-anionic and -cationic compounds: new high entropy materials for advanced Li-ion batteries, Energy Environ. Sci. 12 (8) (2019) 2433–2442, https://doi.org/10.1039/C9EE00368A.
[17] A. Sarkar, L. Velasco, D. Wang, Q. Wang, G. Talasila, L. de Biasi, C. Kübel, T. Brezesinski, S.S. Bhattacharya, H. Hahn, B. Breitung, High entropy oxides for reversible energy storage, Nat. Commun. 9 (1) (2018) 3400, https://doi.org/10.1038/s41467-018-05774-5.
[18] Q. Ding, Y. Zhang, X. Chen, X. Fu, D. Chen, S. Chen, L. Gu, F. Wei, H. Bei, Y. Gao, M. Wen, J. Li, Z.e. Zhang, T. Zhu, R.O. Ritchie, Q. Yu, Tuning element distribution, structure and properties by composition in high-entropy alloys, Nature 574 (7777) (2019) 223–227, https://doi.org/10.1038/s41586-019-1617-1.
[19] A. Sarkar, Q. Wang, A. Schiele, M.R. Chellali, S.S. Bhattacharya, D.i. Wang, T. Brezesinski, H. Hahn, L. Velasco, B. Breitung, High-entropy oxides: fundamental aspects and electrochemical properties, Adv. Mater. 31 (26) (2019) 1806236, https://doi.org/10.1002/adma.201806236.
[20] X. Wang, Q.i. Dong, H. Qiao, Z. Huang, M.T. Saray, G. Zhong, Z. Lin, M. Cui, A. Brozena, M. Hong, Q. Xia, J. Gao, G. Chen, R. Shahbazian-Yassar, D. Wang, L. Hu, Continuous synthesis of hollow high-entropy nanoparticles for energy and catalysis applications, Adv. Mater. 32 (46) (2020) 2002853, https://doi.org/10.1002/adma.202002853.
[21] T.X. Nguyen, J. Patra, J.-K. Chang, J.-M. Ting, High entropy spinel oxide nanoparticles for superior lithiation–delithiation performance, J. Mater. Chem. A 8 (36) (2020) 18963–18973, https://doi.org/10.1039/D0TA04844E.
[22] C.-F. Chang, J.-Y. Chen, G.-M. Huang, T.-Y. Lin, K.-L. Tai, C.-Y. Huang, P.-H. Yeh, W.-W. Wu, Revealing conducting filament evolution in low power and high reliability Fe3O4/Ta2O5 bilayer RRAM, Nano Energy 53 (2018) 871–879, https://doi.org/10.1016/j.nanoen.2018.09.029.
[23] J. Li, G. Johnson, S. Zhang, D. Su, In situ transmission electron microscopy for energy applications, Joule 3 (1) (2019) 4–8, https://doi.org/10.1016/j.joule.2018.12.007.
[24] Z. Yi, Q. Han, X. Li, Y. Wu, Y. Cheng, L. Wang, Two-step oxidation of bulk Sb to one-dimensional Sb2O4 submicron-tubes as advanced anode materials for lithium-ion and sodium-ion batteries, Chem. Eng. J. 315 (2017) 101–107, https://doi.org/10.1016/j.cej.2017.01.020.
[25] Y. Shen, Z. Cao, Y. Wu, Y. Cheng, H. Xue, Y. Zou, G. Liu, D. Yin, L. Cavallo, L. Wang, J. Ming, Catalysis of silica-based anode (de-)lithiation: compositional design within a hollow structure for accelerated conversion reaction kinetics,

J. Mater. Chem. A 8 (25) (2020) 12306–12313, https://doi.org/10.1039/D0TA01671C.
[26] Y. Cheng, Z. Wang, L. Chang, S. Wang, Q. Sun, Z. Yi, L. Wang, Sulfur-mediated interface engineering enables fast SnS nanosheet anodes for advanced lithium/sodium-ion batteries, ACS Appl. Mater. Interfaces 12 (23) (2020) 25786–25797, https://doi.org/10.1021/acsami.0c03860.s001.
[27] K.-L. Tai, C.-W. Huang, R.-F. Cai, G.-M. Huang, Y.-T. Tseng, J. Chen, W.-W. Wu, Atomic-scale fabrication of in-plane heterojunctions of few-layer MoS2 via in situ scanning transmission electron microscopy, Small 16(3) (2020) 1905516. https://doi.org/10.1002/smll.201905516.
[28] T.-Y. Lin, Y.-L. Chen, C.-F. Chang, G.-M. Huang, C.-W. Huang, C.-Y. Hsieh, Y.-C. Lo, K.-C. Lu, W.-W. Wu, L.-J. Chen, In situ investigation of defect-free copper nanowire growth, Nano Lett. 18(2) (2018) 778-784. https://doi.org/10.1021/acs.nanolett.7b03992.
[29] Z. Yang, Z. Zhu, J. Ma, D. Xiao, X. Kui, Y. Yao, R. Yu, X. Wei, L. Gu, Y.-S. Hu, H. Li, X. Zhang, Phase separation of Li2S/S at nanoscale during electrochemical lithiation of the solid-state lithium–sulfur battery using in situ TEM, Adv. Energy Mater. 6 (20) (2016) 1600806. https://doi.org/10.1002/aenm.201600806.
[30] A. Manthiram, A reflection on lithium-ion battery cathode chemistry, Nat. Commun. 11 (1) (2020) 1550, https://doi.org/10.1038/s41467-020-15355-0.
[31] H. Tan, J. Verbeeck, A. Abakumov, G. Van Tendeloo, Oxidation state and chemical shift investigation in transition metal oxides by EELS, Ultramicroscopy 116 (2012) 24–33, https://doi.org/10.1016/j.ultramic.2012.03.002.
[32] H.-Y. Lo, C.-Y. Yang, G.-M. Huang, C.-Y. Huang, J.-Y. Chen, C.-W. Huang, Y.-H. Chu, W.-W. Wu, Observing topotactic phase transformation and resistive switching behaviors in low power SrCoOx memristor, Nano Energy 72 (2020) 104683, https://doi.org/10.1016/j.nanoen.2020.104683.
[33] G. Liang, Z. Wu, C. Didier, W. Zhang, J. Cuan, B. Li, K.-Y. Ko, P.-Y. Hung, C.-Z. Lu, Y. Chen, G. Leniec, S.M. Kaczmarek, B. Johannessen, L. Thomsen, V.K. Peterson, W. K. Pang, Z. Guo, A long cycle-life high-voltage spinel lithium-ion battery electrode achieved by site-selective doping, Angew. Chem. Int. Ed. 59 (26) (2020) 10594–10602, https://doi.org/10.1002/anie.202001454.
[34] D. Chen, C. Feng, Y. Han, B.o. Yu, W. Chen, Z. Zhou, N. Chen, J.B. Goodenough, W. He, Origin of extra capacity in the solid electrolyte interphase near high-capacity iron carbide anodes for Li ion batteries, Energy Environ. Sci. 13 (9) (2020) 2924–2937, https://doi.org/10.1039/C9EE04062E.
[35] M.C. Gao, J.-W. Yeh, P.K. Liaw, Y. Zhang (Eds.), High-Entropy Alloys, Springer International Publishing, Cham, 2016.
[36] E. Lee, J. Blauwkamp, F.C. Castro, J. Wu, V.P. Dravid, P. Yan, C. Wang, S. Kim, C. Wolverton, R. Benedek, F. Dogan, J.S. Park, J.R. Croy, M.M. Thackeray, Exploring lithium-cobalt-nickel oxide spinel electrodes for ≥3.5 V Li-ion cells, ACS Appl. Mater. Interfaces 8 (41) (2016) 27720–27729, https://doi.org/10.1021/acsami.6b09073.
[37] M.R. Chellali, A. Sarkar, S.H. Nandam, S.S. Bhattacharya, B. Breitung, H. Hahn, L. Velasco, On the homogeneity of high entropy oxides: an investigation at the atomic scale, Scripta Mater. 166 (2019) 58–63, https://doi.org/10.1016/j.scriptamat.2019.02.039.
[38] D. Luo, S. Fang, Y. Tamiya, L. Yang, S.-i. Hirano, countering the segregation of transition-metal ions in LiMn1/3Co1/3Ni1/3O2 cathode for ultralong life and high-energy li-ion batteries, Small 12(32) (2016) 4421-4430. 10.1002/smll.201601923.
[39] D.A. Andersson, C.R. Stanek, Mixing and non-stoichiometry in Fe–Ni–Cr–Zn–O spinel compounds: density functional theory calculations, Phys. Chem. Chem. Phys. 15 (37) (2013) 15550–15564, https://doi.org/10.1039/C3CP50312G.
[40] M. Soliman Selim, G. Turky, M.A. Shouman, G.A. El-Shobaky, Effect of Li2O doping on electrical properties of CoFe2O4, Solid State Ionics 120 (1) (1999) 173–181, https://doi.org/10.1016/S0167-2738(99)00008-9.
[41] T.L. Daulton, B.J. Little, Determination of chromium valence over the range Cr(0)–Cr(VI) by electron energy loss spectroscopy, Ultramicroscopy 106 (7) (2006) 561–573, https://doi.org/10.1016/j.ultramic.2006.02.005.
[42] Y.-M. Kim, J. He, M.D. Biegalski, H. Ambaye, V. Lauter, H.M. Christen, S. T. Pantelides, S.J. Pennycook, S.V. Kalinin, A.Y. Borisevich, Probing oxygen vacancy concentration and homogeneity in solid-oxide fuel-cell cathode materials on the subunit-cell level, Nat. Mater. 11 (10) (2012) 888–894, https://doi.org/10.1038/nmat3393.
[43] S.G. Bratsch, Standard electrode potentials and temperature coefficients in water at 298.15 K, J. Phys. Chem. Ref. Data 18 (1) (1989) 1–21, https://doi.org/10.1063/1.555839.
[44] W. Guo, Z. Wang, J.u. Li, Diffusive versus displacive contact plasticity of nanoscale asperities: temperature- and velocity-dependent strongest size, Nano Lett. 15 (10) (2015) 6582–6585, https://doi.org/10.1021/acs.nanolett.5b02306.
[45] Z. Zhu, R. Gao, I. Waluyo, Y. Dong, A. Hunt, J. Lee, J.u. Li, Stabilized Co-free Li-rich oxide cathode particles with an artificial surface prereconstruction, Adv. Energy Mater. 10 (35) (2020) 2001120, https://doi.org/10.1002/aenm.202001120.
[46] Y. Shen, H. Xue, S. Wang, D. Zhang, D. Yin, L. Wang, Y. Cheng, Ammonia-low coprecipitation synthesis of lithium layered oxide cathode material for high-performance battery, Chem. Eng. J. 411 (2021) 128487, https://doi.org/10.1016/j.cej.2021.128487.

Atomic-scale Investigation of Lithiation/Delithiation Mechanism in High-entropy Spinel Oxide with Superior Electrochemical Performance

Chih-Yang Huang [a], Chun-Wei Huang [b], Min-Ci Wu [a], Jagabandhu Patra [c], Thi Xuyen Nguyen [d], Mu-Tung Chang [b], Oliver Clemens [e], Jyh-Ming Ting [d,], Ju Li [f], Jeng-Kuei Chang [a,*] and Wen-Wei Wu [a,g,h,*]*

[a] Department of Materials Science and Engineering, National Chiao Tung University, Hsinchu 30010, Taiwan

[b] Material and Chemical Research Laboratories, Industrial Technology Research Institute, Hsinchu 31040, Taiwan

[c] Hierarchical Green-Energy Materials (Hi-GEM) Research Center, National Cheng Kung University, Tainan 70101, Taiwan

[d] Department of Materials Science and Engineering, National Cheng Kung University, Tainan 70101, Taiwan

[e] Universität Stuttgart, Institut für Materialwissenschaft, Chemische Materialsynthese, Heisenbergstraße 3, 70569, Stuttgart, Germany.

[f] Department of Nuclear Science and Engineering and Department of Materials Science and Engineering, Massachusetts Institute of Technology, Cambridge, MA 02139, USA

[g] Intelligent Semiconductor Nanosystem Technology Research Center, Hsinchu 30078, Taiwan

[h] Frontier Research Center on Fundamental and Applied Sciences of Matters, National Tsing Hua University, Hsinchu 30013, Taiwan

[*] Corresponding authors:

Email: wwwu@mail.nctu.edu.tw (Wen-Wei Wu)

jkchang@nctu.edu.tw (Jeng-Kuei Chang)

jting@mail.ncku.edu.tw (Jyh-Ming Ting)

List of Contents.

Supplementary tables

Supplementary figures

Table S1. Rietveld refinement data for HEO. The XRD pattern was fitted using a single phase spinel structure. Site occupancies fixed from ICP analysis.

Phase			Spinel			
R-Bragg			2.2 %			
Space-group			*Fd*-3*m*			
Crystallite size (nm)			14.7(4)			
Lattice parameter (Å)			8.346(2)			
Label	Wyckoff site	x	y	z	Atom	Occupation
Anion	32*e*	0.2467(7)	=x	=x	O	1
Oct.	16c	0	0	0	Fe	0.08
					Cr	0.112
					Mn	0.286
					Ni	0.22
					Co	0.302
Tetr.	8b	3/8	3/8	3/8	Cr	0.112
					Ni	0.22
					Co	0.302
					Mn	0.286
					Fe	0.08

Table S2. The formation energy of binary spinel oxides.

Oxide system	Formation energy (eV)	Reference
$Cr_xFe_{3-x}O_4$	-15.13	39
$Ni_xCr_{3-x}O_4$	-14.21	39
$Ni_xFe_{3-x}O_4$	-10.48	39
$Co_xFe_{3-x}O_4$	+0.59	40

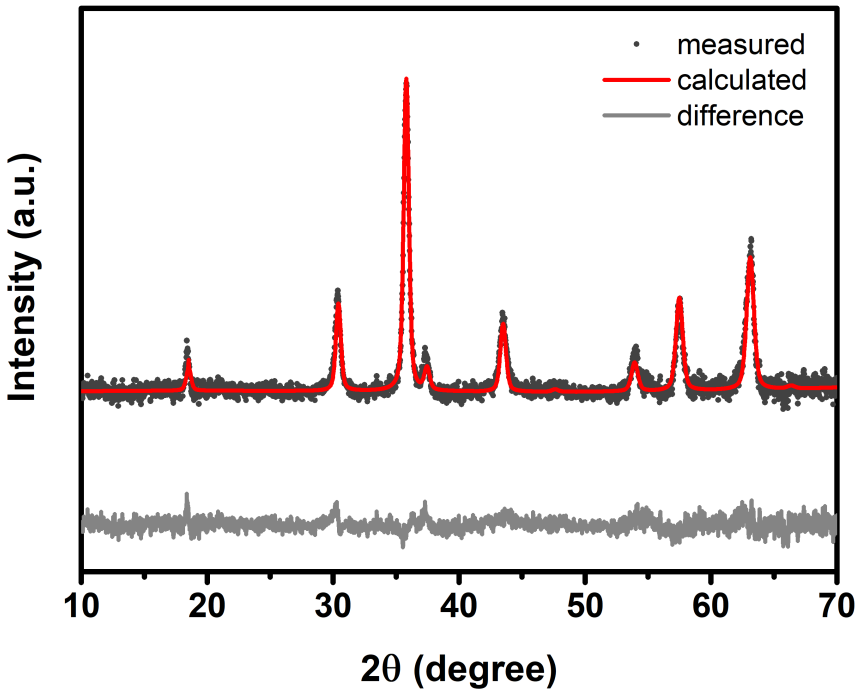

Figure S1. XRD patterns of HEO and the corresponding Rietveld fitting. Rietveld analysis has been done using program TOPAS 6 on the raw data in an angular range between 10° to 70° 2θ. The pattern has been fitted with a single cubic spinel phase (Fd-3m). Due to the indistinguishability of the different transition metals, their site occupancies were taken as determined from ICP analysis, without considering the possibility for site ordering for the tetrahedrally and octahedrally coordinated sites. A Voigt function with $\cos^{-1}(\theta)$ angular dependence was used to model the intensity distribution of the reflections, and the crystallite size was determined from the integral breadth of the reflections.

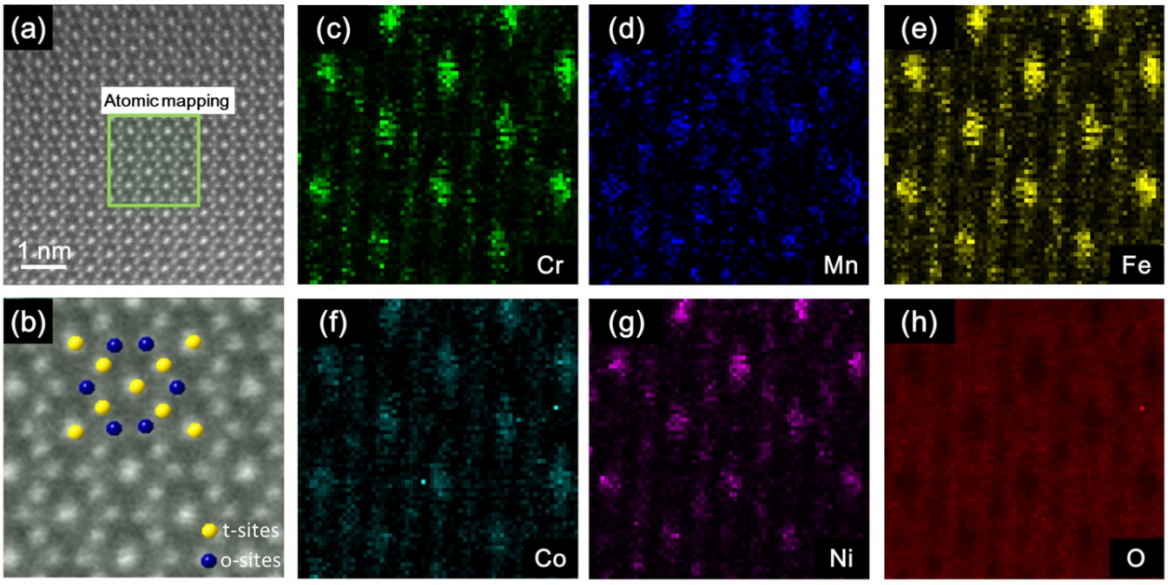

Figure S2. Identification of multi-cations atomic positions. (a) HRSTEM image of pristine

HEO in zone of [110]. (b) Enlarged HRSTEM image to show the occupying sites in HEO. (c-h) EELS mapping analysis of Cr, Mn, Fe, Co, Ni and O, respectively.

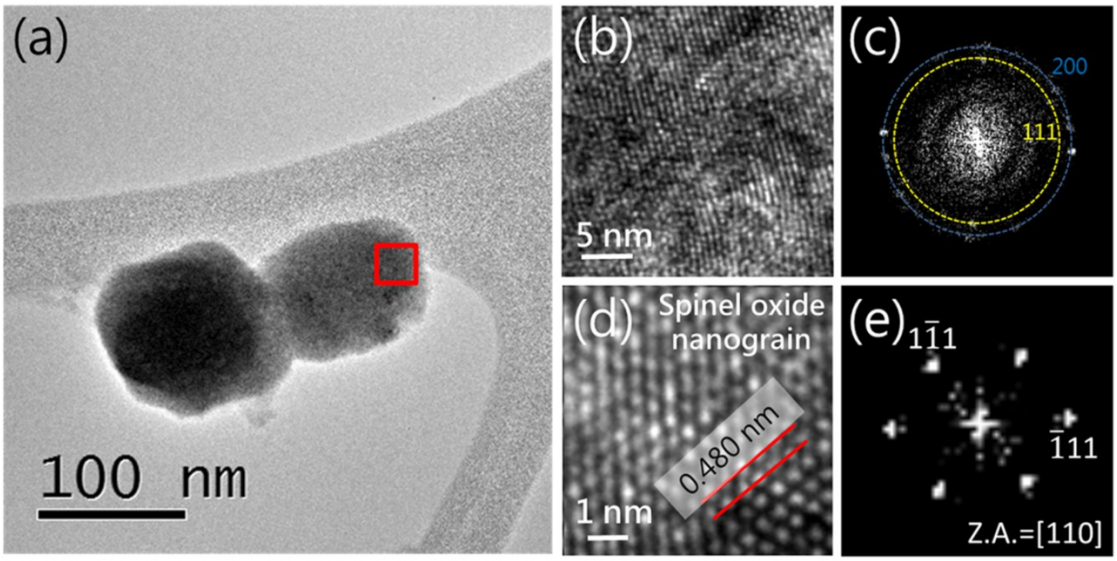

Figure S3. Structure identification of HEO particles after 0.01-V lithiation. (a) TEM image of lithiated HEO particles. (b) HRTEM image and (c) corresponding FFT pattern of spinel oxide nanograins. (d) HRTEM image and (e) corresponding FFT pattern of a single spinel nanograin.

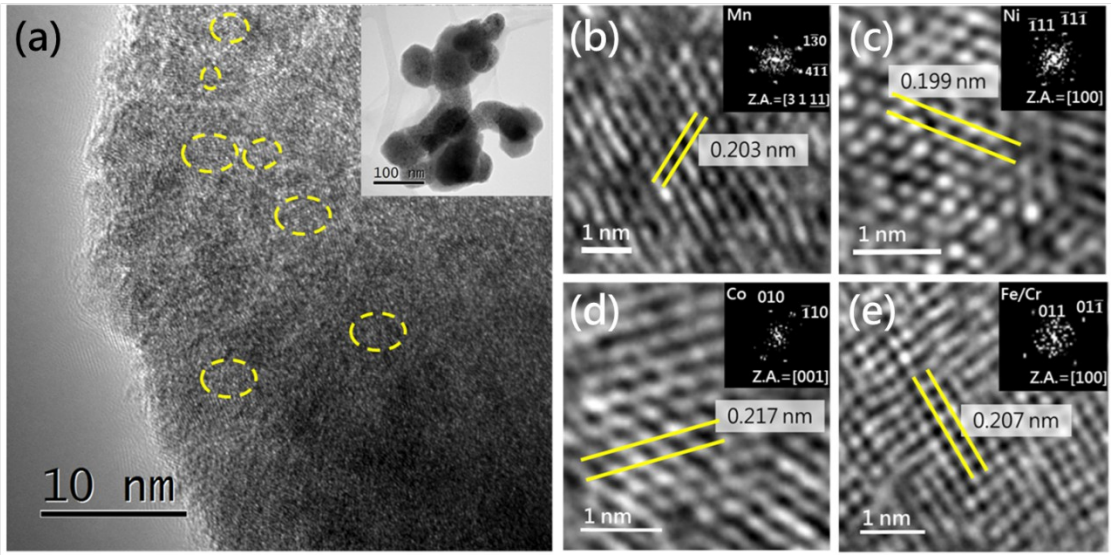

Figure S4. Structure identification of HEO particles after second lithiation. (a) TEM image of HEO particles after second lithiation. HRTEM images of (b) Mn, (c) Ni, (d) Co, and (e) Cr/Fe nanocrystals.

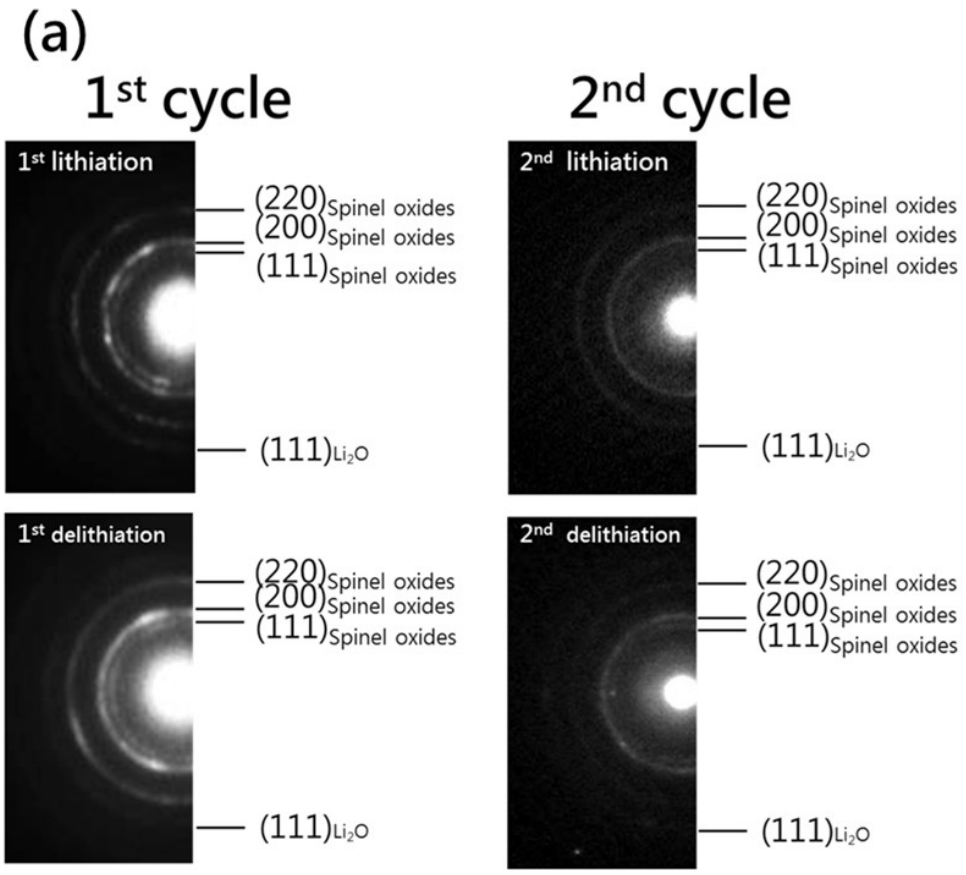

(b)	HEO	$Cr_xFe_{3-x}O_4$	$Li_2Co_xNi_{1-x}O_2$
a (Å)	8.355	8.387	8.007
(111)	4.824	4.842	4.623
(200)	4.178	4.194	4.004
(220)	2.954	2.965	2.831

Figure S5. Electron diffraction patterns during charging-discharging cycles. (a) Diffraction patterns of HEO samples after lithiation and delithiation at the first and second cycles. (b) Lattice constants and *d* spacing values of pristine spinel HEO, $Cr_xFe_{3-x}O_4$, and $LiNi_xCo_{1-x}O_2$ phases.

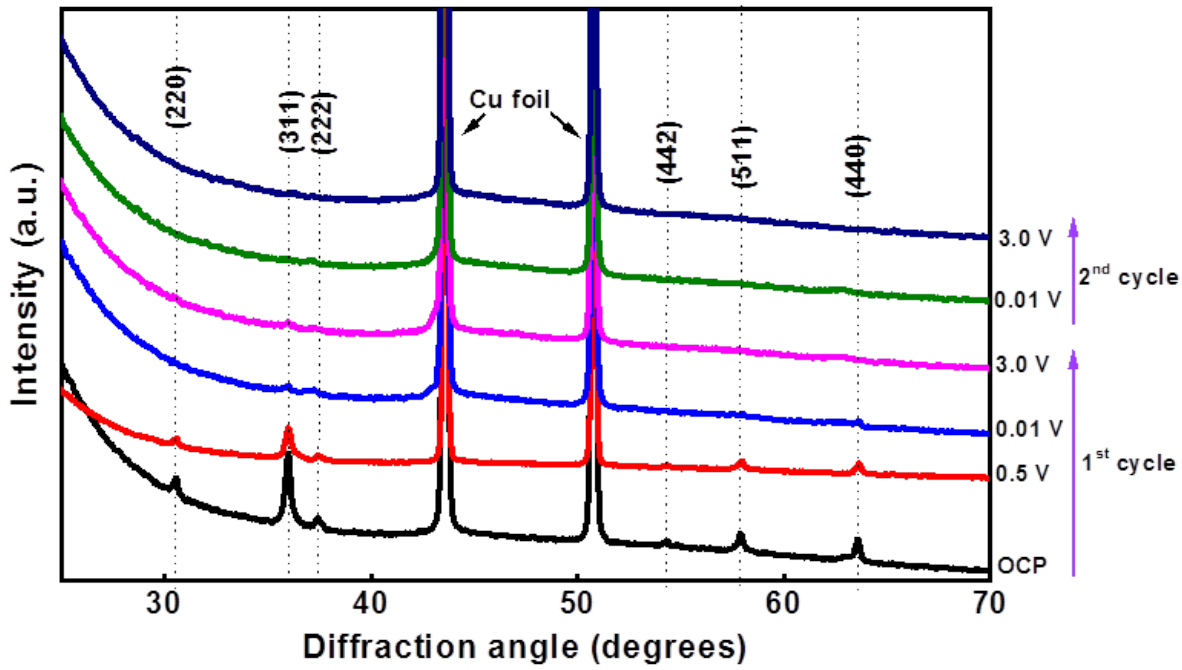

Figure S6. The XRD patterns of different states to show the macro-scale crystallinity.

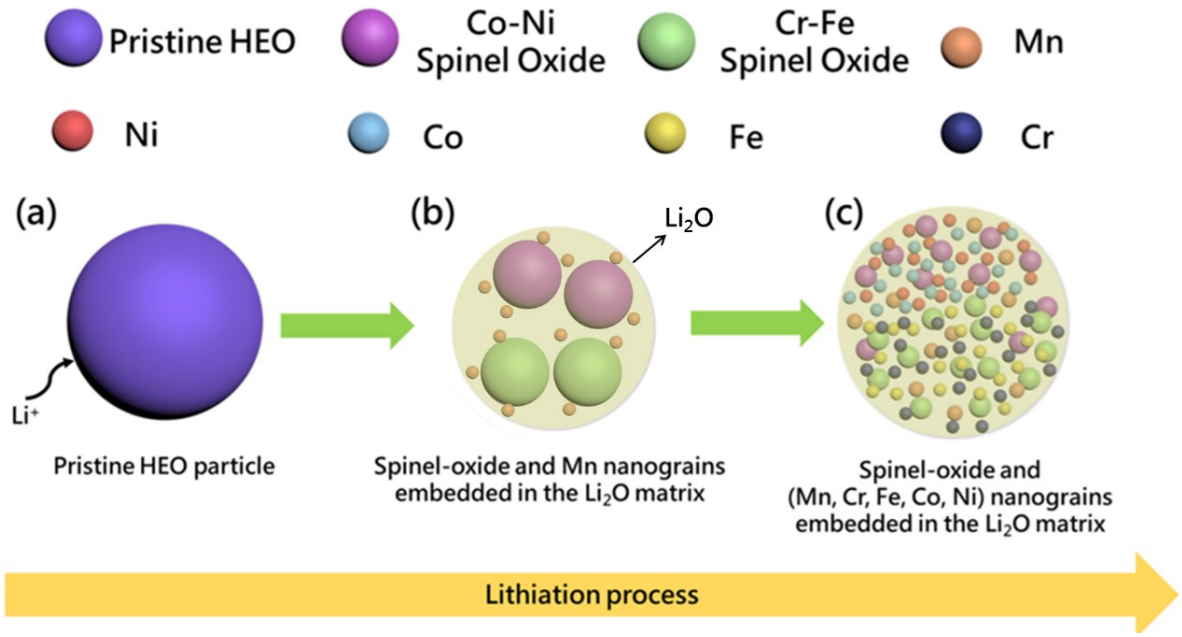

Figure S7. Schematic illustration of macroscale structural transition of HEO during

lithiation.

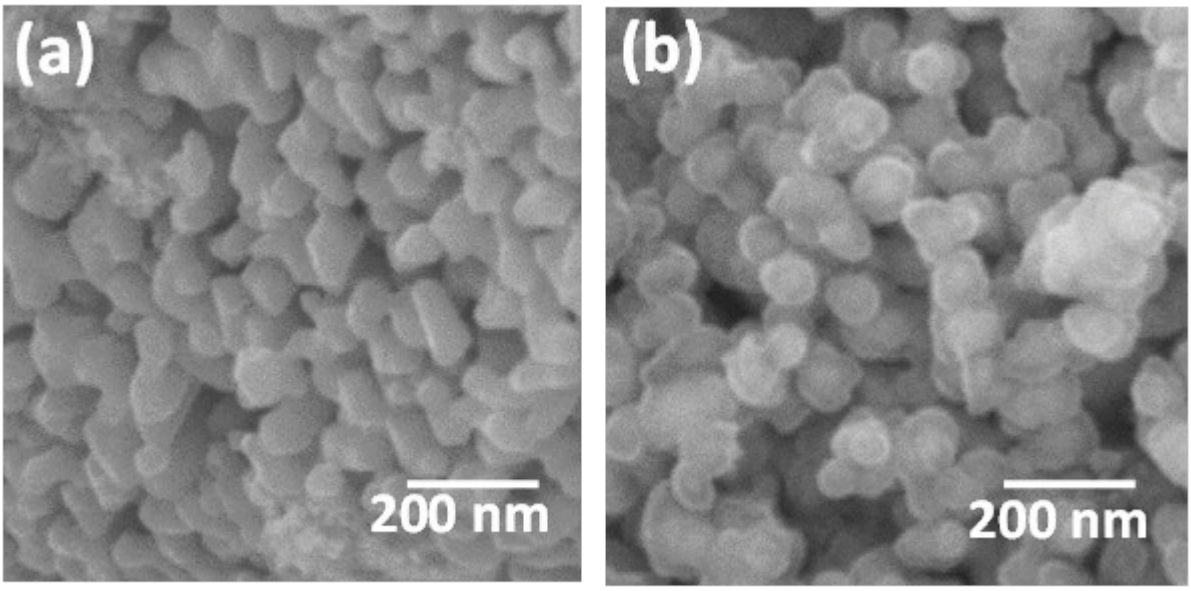

Figure S8. Morphology change of HEO particles after cycling. SEM images of HEO electrodes (a) before and (b) after 100 charge-discharge cycles (terminated at lithiation step).

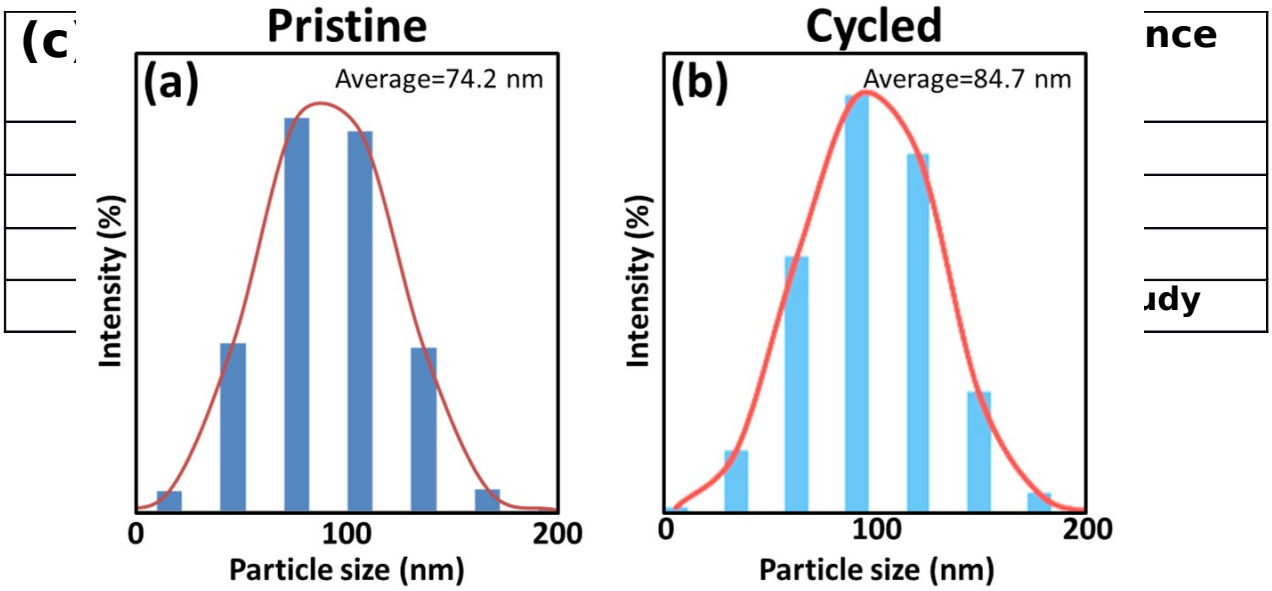

Figure S9. Diameter expansion of HEO particles after lithiation. Particle size distribution of (a) pristine particles and (b) particles after 100 cycles (terminated at lithiation step). (c) Diameter expansion comparison between our HEO and conventional transition metal oxides reported in the literature.

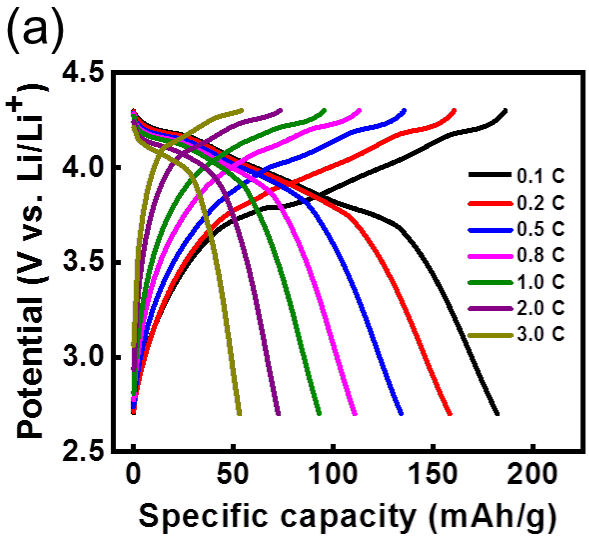

(b)

Rate (C)	Capacity (mAh/g)
0.1	182/186
0.2	158/160
0.5	134/136
0.8	111/113
1.0	93/95
2.0	72/73
3.0	53/54

Figure S10. The full battery test. (a) The charge-discharge curves of full cell at various current densities. (b) The chart of the capacities measured in (a).